

Processing of high performing composite cathodes for protonic ceramic fuel cells by exsolution

Received 00th January 20xx,
Accepted 00th January 20xx

Laura Rioja-Monllor^{a,c}, Carlos Bernuy-Lopez^{a,c}, Marie-Laure Fontaine^b, Tor Grande^a and Mari-Ann Einarsrud^a

DOI: 10.1039/x0xx00000x

www.rsc.org/

La_{0.5}Ba_{0.5}CoO_{3-δ}-BaZrO₃ (LB-BZ)-based composite materials were prepared by a modified Pechini sol-gel method combined with exsolution. Two different LB-BZ composites were prepared through two alternative thermal treatments of the precursor gel. A metastable single phase with perovskite crystal structure was first obtained upon annealing the precursor in inert atmosphere, which further transformed to a two-phase composite by *in situ* exsolution in air. Comparatively, direct calcination of the LB-BZ gel in air resulted in a two-phase composite with different microstructure and composition of the two phases. The composite cathode formed by exsolution consisted of a matrix of BZ-phase with ~45 nm grain size embedding ~20 nm grains of LB-phase, while the composite cathode obtained by direct calcination consisted of a mixture of both phases with 50-60 nm grain size. Electrodes of symmetric half-cells were spray-coated on BaZr_{0.9}Y_{0.1}O_{2.95} electrolytes to examine the electrochemical performance by impedance spectroscopy. The lowest area specific resistance (ASR) was obtained for the composite cathode produced by exsolution with an excellent ASR of 1.54 Ω cm² at 600 °C, 18 Ω cm² at 400 °C and an activation energy (E_a) of 0.60 eV in 3 % moist synthetic air. This work demonstrates the potential of fabricating high performance nanocomposite cathodes with tailored chemical composition by a novel exsolution method.

Introduction

Solid oxide fuel cells (SOFCs) receive considerable interest as they offer one of the most efficient electrochemical energy conversion directly into electrical power. Traditional SOFCs with oxygen ion conducting electrolytes require operation at higher temperatures due to the low ionic conductivity of the electrolyte at lower temperatures. High operation temperature imposes restrictions on material compatibility resulting in high costs, material degradation, thermal expansion coefficient mismatch, slow start-up and shut-off, etc ¹. In addition, the production of water at the fuel side increases the complexity of the system due to the need for recirculation of fuel and water management ¹. Alternatively, protonic ceramic fuel cells (PCFCs) can operate at lower temperature because of the lower activation energy for proton conduction compared to oxygen ion conductivity ². Efforts nowadays are focused on cathode material development in PCFCs, which are presently dominating the performance of the cells ^{3,4}. Therefore, the development of highly electrochemically active cathodes for PCFCs requires the optimization of material compositions as well as microstructures together with a better understanding of electrode processes.

The cathode can be made of a mixed electronic and ionic conductor (MIEC) showing good catalytic activity for oxygen reduction, high electronic conductivity and chemical stability towards the electrolyte material. Furthermore, a composite made of an ionic and electronic conductor offers cathodes with high electrical conductivity, low area specific resistivity (ASR)

and superior electrocatalytic properties in order to reduce the polarization resistance ⁵.

Materials containing 3d transition metals have generally excellent properties with respect to kinetics of the oxygen reduction reaction (ORR) ⁶. Since the operating temperature for PCFCs is in the 400-700 °C range, conventionally used intermediate temperature-SOFC single phase perovskite cathode materials such as Ba_{0.5}Sr_{0.5}Co_{0.8}Fe_{0.2}O_{3-δ} (BSCF) ⁷, La_{0.6}Sr_{0.4}Co_{0.2}Fe_{0.8}O_{3-δ} (LSCF) ^{8,9} and La_{1-x}Ba_xCoO_{3-δ} (LBC) ¹⁰⁻¹² have interesting properties as cathodes for PCFC. Moreover, perovskite materials with composition Ln_{0.5}Ba_{0.5}MO_{3-δ} (Ln = La, Y, Gd and M = Co, Fe, Mn) are known to have a good oxygen ion and electronic conductivity and can therefore, directly be used as cathode materials for PCFC even though no proton conductivity has been demonstrated ^{11,13}.

The introduction of proton conductivity in the cathode is necessary in order to increase the performance. Proton conduction along the cathode extends the reaction sites to the entire cathode-gas interface ¹⁴. Hence, attractive cathode materials may combine oxygen ion, protonic and electronic conduction. These may likely be achieved by designing the electrode as ceramic-ceramic composite ⁵. For instance, composite cathodes could be a combination of an oxide with high electronic and oxygen ion conductivities (as for instance those found in the literature for SOFC application) and another oxide with high proton conductivity, which can be as well, the chosen electrolyte material. This would further contribute to improve adhesion of the electrode and reduce potential thermal mismatch between the electrolyte and the electrode. There are many pathways for preparing composite electrodes. Among these, infiltration methods have shown promising results. A mixed oxygen ion and electron conductor infiltrated into a porous backbone of a proton conductor has been studied as cathode materials ⁹. Pure electronic conductor (e.g. LaCoO₃) ¹⁵, oxygen ion and electronic conductor (e.g. LSCF) ⁹ and triple oxygen ion/protonic/electronic conductor (e.g. BaCo_{0.4}Fe_{0.4}Zr_{0.1}Y_{0.1}O_{3-δ}) ^{3,16} cathodes infiltrated into a proton conducting oxide backbone have been recently reported.

^a Department of Materials Science and Engineering, NTNU Norwegian University of Science and Technology, 7491 Trondheim, Norway; mari-ann.einarsrud@ntnu.no (M.-A.E.); tor.grande@ntnu.no (T.G.).

^b SINTEF Industry, 0314 Oslo, Norway. Marie-laure.fontaine@sintef.no

^c Current address: Sandvik Materials and Technology, R&D, Sandviken, Sweden. Laura.rioja-monllor@sandvik.com (L.R.-M.) carlos.bernuy-lopez@sandvik.com (C.B.-L.).

Electronic Supplementary Information (ESI) available: [details of any supplementary information available should be included here]. See DOI: 10.1039/x0xx00000x

Several critical issues still remain to be solved on the infiltration technique. Challenges are frequently observed during the fabrication of the cathode layer due to chemical instability or from the reactivity of the infiltrated material with the other components at the firing temperature. The long-term stability of these cathodes is yet to be demonstrated due to degradation of the infiltrated nanoparticles¹⁷. Mechanical mixtures of typical SOFC cathode and the electrolyte materials have also been investigated but an improvement of the microstructure of the cathode is needed. A link between the microstructure and the electrochemical performance has been reported to be due to the low number of active sites, limited gas diffusion or limited adhesion to the electrolyte^{18,19}.

In an effort to enhance the properties of PCFC cathodes, a novel synthesis approach based on *in situ* driven decomposition of a precursor oxide by exsolution and the possibility to induce phase decomposition by red-ox chemistry has been demonstrated in our group²⁰ and recently applied to demonstrate the good performance of nanocomposite cathodes for PCFC²¹. The exsolution of nanoparticles is attracting much attention in the design of electrodes and exsolution of nanoparticles such as nickel, ruthenium or other catalyst metals has been investigated in reducing conditions for the preparation of PCFC and SOFC anodes²²⁻²⁵. Further developing this approach to form ceramic-ceramic composite cathodes will open a new path to manufacture efficient electrodes²¹. This reaction pathway may open up for composites with interesting microstructural features such as bimodal size distribution of the phases and adjustable composition depending on the processing parameters.

In this work, we present a novel exsolution route to $\text{La}_{0.5}\text{Ba}_{0.5}\text{CoO}_{3-\delta}$ - BaZrO_3 -based composites, recently utilized to fabricate high performance composite cathodes²¹. Two novelties are presented in this work; the exsolution of complex materials and the oxidizing induced exsolution, matching the cathode operating conditions. In addition, this method will enable BaZrO_3 to have sufficient oxygen vacancies and therefore proton conductivity. We demonstrate that the microstructure of the composite and the chemical composition of the two phases can be tailored by optimization of the thermal treatment. A thorough description of the synthesis and reaction mechanisms are presented as well as a careful characterization of the microstructure and phase composition of the composite electrodes. Finally, the electrochemical performance of the new composites as cathodes for PCFC with BaZrO_3 -based electrolyte is demonstrated.

Experimental

Synthesis and symmetric cell preparation

Nanocomposite electrodes of nominal composition $0.6 \text{La}_{0.5}\text{Ba}_{0.5}\text{CoO}_{3-\delta} - 0.4 \text{BaZrO}_3$ were prepared by a modified Pechini method followed by *in situ* oxidation driven decomposition of a precursor oxide by exsolution into the composite.

All the starting materials were bought from Sigma-Aldrich (Steinheim, Germany). The cation precursors for the synthesis

of the composites were barium nitrate ($\text{Ba}(\text{NO}_3)_2$, > 99.999 %), lanthanum nitrate hexahydrate ($\text{La}(\text{NO}_3)_3 \cdot 6\text{H}_2\text{O}$, > 99.99 %), zirconyl nitrate hydrate ($\text{ZrO}(\text{NO}_3)_2 \cdot x\text{H}_2\text{O}$, > 99 %) and cobalt nitrate hydrate ($\text{Co}(\text{NO}_3)_2 \cdot 6\text{H}_2\text{O}$, > 99.999 %). Ethylenediaminetetraacetic acid (EDTA, > 99 %) as well as citric acid (CA, > 99 %) were used as complexing agents. Aqueous lanthanum, zirconium and cobalt precursor solutions of approximately $3 \cdot 10^{-4}$ mol cations/g were individually standardized by thermogravimetric analysis.

The scheme of the synthesis route is shown in Figure 1. EDTA (8.9231 g) was dissolved in ~20 mL of NH_4OH solution (pH=10.5) to which citric acid pre-dissolved in an aqueous solution (11.7322 g) was added. Stoichiometric amounts of cations were added to this solution as described below to give the nominal $\text{La}_{0.3}\text{Ba}_{0.7}\text{Zr}_{0.4}\text{Co}_{0.6}\text{O}_{3-\delta}$ composition. In this order, barium nitrate, lanthanum and cobalt precursor solutions were added to the EDTA/citric acid solution. The solution was adjusted to pH=6.5 with dilute nitric acid. Thereafter, zirconium precursor solution was added dropwise with a flow of 1 mL/min to avoid any precipitation due to pH mismatch. The molar ratio between EDTA: citric acid: total metal cation was 1.5:3:1. The resulting sol with pH=5.5 was heated in air on a hot plate at 120 °C until gelation occurred.

The gel was further dried in air for 12 h at 200 °C to form a solid porous structure (xerogel). The xerogel was ground in a mortar and calcined in air at 450 °C for 24 h in order to decompose the organic compounds. The precursor powder was further ground in a mortar and compacted by uniaxial pressing at 50 MPa. The pellets were annealed in N_2 atmosphere at 715 °C for 8 h in order to achieve a single phase (SP) $\text{La}_{0.3}\text{Ba}_{0.7}\text{Zr}_{0.4}\text{Co}_{0.6}\text{O}_{3-\delta}$ material. The pellets were further crushed and pressed at 50 MPa and calcined in ambient air at 900 °C for 6 h in order to

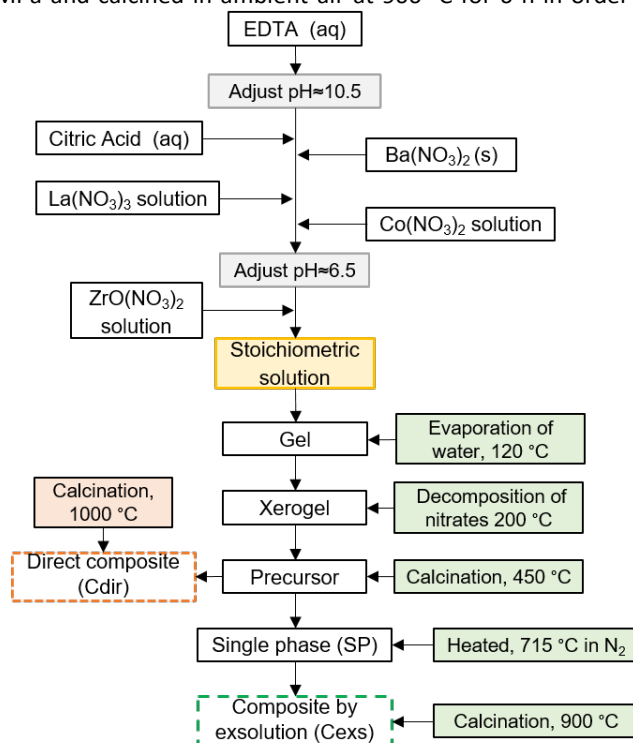


Figure 1. Flow chart of the modified Pechini synthesis of $\text{La}_{0.5}\text{Ba}_{0.5}\text{CoO}_{3-\delta}$ - BaZrO_3 -based composites. The precursor is heated in N_2 to form a single phase prior the exsolution into the composite by exsolution at 900 °C in air. The direct composite is prepared by calcination of the precursor at 1000 °C in air.

exsolute the SP into nominal composition $\text{La}_{0.5}\text{Ba}_{0.5}\text{CoO}_{3-\delta}$ - BaZrO_3 composite (Cexs). As a reference, $\text{La}_{0.5}\text{Ba}_{0.5}\text{CoO}_{3-\delta}$ - BaZrO_3 composite was also prepared by direct calcination of the compacted precursor at 1000 °C for 6 h to form a composite material (Cdir). An explanation on the phase formation and exsolution method is given in the discussion part. All the thermal treatments were performed using 2 °C/min cooling and heating rate.

$\text{BaZr}_{0.9}\text{Y}_{0.1}\text{O}_{2.95}$ (BZY10) electrolyte supported symmetric cells with the cathode material were prepared as follows. BZY10 powder was prepared by spray-pyrolysis (CerPoTech AS, Tiller, Norway, purity > 99 %) of a mixture of nitrate solutions containing stoichiometric amounts of the cations. Dense samples were prepared by solid state sintering as described by Sazinas et al.²⁶. Green cylindrical pellets (diameter 10 mm) were made by uniaxial pressing at 100 MPa with subsequent cold isostatic pressing (CIP) at 200 MPa. The sintering of the pellets was performed at 1600 °C for 10 h in ambient air with 10 °C/min heating rate. The surface was ground with SiC papers. For the preparation of electrodes, Cexs and Cdir powders were dispersed in ethanol using 5 wt.% solid content and an addition of 3 wt.% Dolacol D 1003 (Zschimmer & Schwarz GmbH) as a dispersant. The dispersion was deposited by spray coating on both sides of the BZY10 electrolyte pellets. The symmetric cells were fired at 900 °C for 4 h (Cexs) or at 1000 °C for 3 h (Cdir) in ambient air to form porous cathode layers of ~20 µm thickness. The lower firing temperature of the Cexs cathode was chosen not to exceed the temperature for the exsolution. Platinum paste was applied onto the cathodes as a current collector and platinum was employed as a conducting wire.

Bars of Cexs and Cdir were made for electrical conductivity measurement using 50 mm x 10 mm die with a uniaxial pressing at 50 MPa and subsequent cold isostatic pressing at 200 MPa. The bars were sintered for 12 h at 1000 °C for Cdir and at 900 °C for Cexs.

Characterization

The prepared materials were analyzed after each synthesis step by X-ray diffraction (XRD) using a Bruker D8 DaVinci equipped with Lynxeye™ detector and $\text{CuK}\alpha$ radiation. High temperature X-ray diffraction (HTXRD) was performed by Bruker D8 ADVANCE diffractometer equipped with $\text{CuK}\alpha$ radiation and a VANTEC-1 position sensitive detector. The powders were placed on a Pt-strip sample holder mounted within a high temperature camera (MRI TCP20). The sample temperature was calibrated using a corundum standard. The precursor powder was heated in synthetic air and diffractograms were recorded from 450 to 850 °C every 50 °C and further every 10 °C from 865 to 975 °C. The precursor powder was also studied in N_2 atmosphere upon heating from 430 to 740 °C scanning every 50 °C. The exsolution of the single phase was investigated in synthetic air by heating the single phase from 430 to 740 °C with a recording every 30 °C. A delay time of 300 s was set before each diffractogram for the equilibration of the temperature. Unit cell parameters were refined by Rietveld method using Bruker AXS TOPAS software

v4.2. The peak shape for each pattern was described using a modified Thomson-Cox-Hastings pseudo-Voigt (PV-TCHZ).

The microstructure of SP, Cexs and Cdir was examined by scanning in-lens cold field emission electron microscopy (S(T)EM, Hitachi S-5500). Dispersions of SP, Cexs and Cdir in ethanol were dropped on holey carbon coated copper grids for transmission electron microscopy (TEM). TEM images were recorded on a JEOL JEM-2100F with an accelerating voltage of 200 kV equipped with an Oxford X-Max 80 SDD EDX. The chemical composition of the composites was estimated by EDX analysis in combination with Rietveld refinements. The microstructure and the grain size of the composites was studied by high resolution images (HR-TEM) analysis of 52 grains for Cexs and 119 grains for Cdir. The d_{hkl} distances were measured by extracting an area of interest from the HR-TEM images with fast Fourier transform analysis, and calculating the average distance over more than ten consecutive hkl planes, using DigitalMicrograph with Gatan Microscopy Suite (GMS 3) software. See supplementary information Figure S1 for further information about how the grain size was calculated. The specific surface area of the composites was measured by nitrogen adsorption, according to Brunauer-Emmett-Teller (BET) theory, on a Micromeritics Tristar 3000 analyzer.

Thermogravimetric analysis (TGA) of the gel was carried out in air using Netzsch STA 449C with heating rate of 2 °C/min from room temperature to 1000 °C. Total electrical conductivity measurements in synthetic air, O_2 and N_2 were performed by DC-conductivity in a 4-point 4-wire setup applying a constant voltage of 1.48 V. Cexs and Cdir bars of about 22 mm x 5 mm x 2.5 mm were measured. Platinum wires were mounted onto the ends measuring approximately 10 mm between the current electrodes and 5 mm between the voltage electrodes. Cexs bar with 50% density and Cdir bar with 70% were heated to 800 °C with 2 °C/min ramp and data was collected during cooling for each 100 °C after 2 h dwell.

Electrochemical impedance spectroscopy (EIS) of symmetrical cells was measured in dry and moist ($p_{\text{H}_2\text{O}} = 0.03$ atm) synthetic air from 400 to 600 °C, in temperature intervals of 50 °C (with a cooling rate of 1 °C/min and 6 h dwell before measurement) using a ProboStat™ (NorECs AS, Norway) set-up and an Alpha A (Novocontrol Technologies) impedance analyzer. The signal amplitude was 50 mV under open circuit voltage (OCV) in the 10^{-2} - 10^6 Hz frequency range. The 3 % moist atmosphere was achieved by bubbling synthetic air through distilled water at 25 °C. Experimental data was refined using Zview software v3.5 (Scribner).

Results

A modified Pechini sol-gel route was first developed to prepare a single phase material with the complex stoichiometry $\text{La}_{0.3}\text{Ba}_{0.7}\text{Zr}_{0.4}\text{Co}_{0.6}\text{O}_{3-\delta}$. The pH and temperature were optimized to obtain a homogeneous gel with EDTA: citric acid: total metal cation ratio of 1.5:3:1 without any visible precipitation. The thermogravimetric analysis of the amorphous xerogel in Figure 2 shows two mass losses during thermal treatment. The first step corresponds to the partial decomposition of the metal-complexes from 200 to 360 °C and is slightly exothermic. The

second mass loss is centered at 418 °C and is strongly exothermic. This feature is attributed to the pyrolysis of nitrate/citrate/EDTA organic materials. No significant mass loss occurred above 425 °C.

XRD patterns at room temperature of the materials after each synthesis step are provided in Figure 3. The xerogel was amorphous after drying at 200 °C, while after calcination in air at 450 °C, the presence of crystalline BaCO₃ is clearly evident. By heating this powder further in N₂ at 715 °C, a single phase perovskite with a cubic structure (*Pm-3m*) was obtained. Further annealing in air at 900 °C resulted in the formation of a composite (Cexs) consisting of a La_{0.5}Ba_{0.5}CoO_{3-δ} and a BaZrO₃-based phase. As an alternative to this route, direct calcination in air of the precursor at 1000 °C gave a composite (Cdir) consisting of two similar phases according to XRD. No other reflections beside those belonging to these two phases are evident in the 5-75° 2θ range.

In situ HTXRD patterns displayed in Figure 4 revealed the mechanisms for the evolution of the phase formation of the two composite cathodes obtained by the two different thermal treatments. For the composite by exsolution (Figure 4a), the precursor calcined at 450 °C was annealed in N₂ in order to form the single phase and was the starting material for HTXRD experiment. The thermal evolution of the La_{0.3}Ba_{0.7}Zr_{0.4}Co_{0.6}O_{3-δ} single phase in synthetic air shows a sharpening of the diffraction lines at 800 °C prior to the exsolution. The diffraction lines of the two phases present in the composite became significantly broadened above 800 °C due to the exsolution. Figure 4b shows the formation mechanism of the Cdir directly from the precursor calcined at 450 °C containing BaCO₃. After complete decomposition of BaCO₃ in the amorphous oxide at 538 °C, a transient phase is observed at 641 °C prior the formation of the composite at 800 °C. A thermal treatment of the precursor at 750 °C in synthetic air was conducted in order to study the transient phase. This transient perovskite phase is only stable at high temperatures and decomposes at room temperature. Reflections of different hexagonal BaCoO_x polymorphs were observed by XRD (Supplementary data, Figure

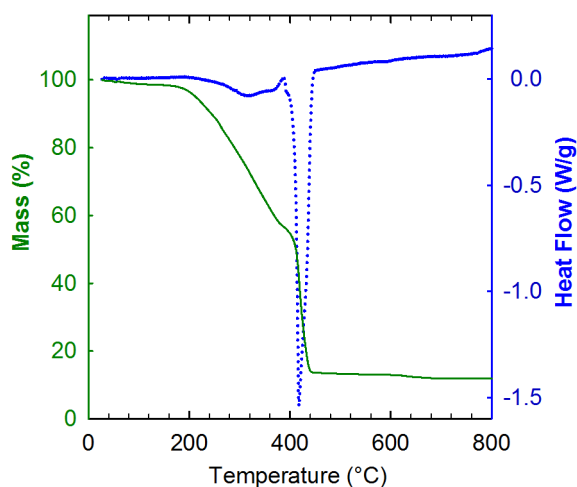


Figure 2. Thermogravimetric analysis and differential scanning calorimetry of the amorphous xerogel with La_{0.5}Ba_{0.5}CoO_{3-δ} - BaZrO₃ nominal composition in synthetic air.

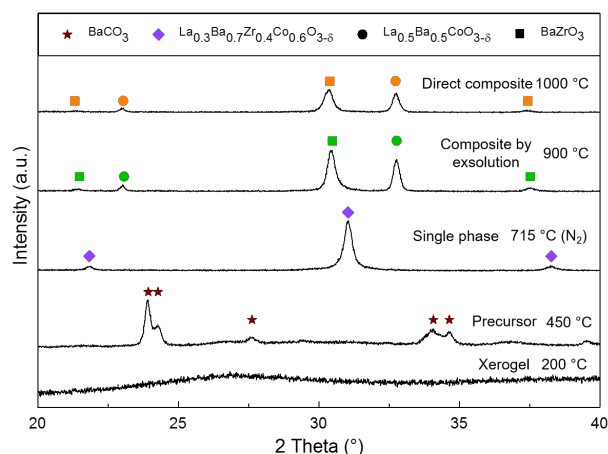


Figure 3. Tracking of the synthesis by X-ray diffraction at room temperature after each synthesis step. La_{0.3}Ba_{0.7}Zr_{0.4}Co_{0.6}O_{3-δ} - BaZrO₃ xerogel is formed at 200 °C and a precursor is formed at 450 °C after the decomposition of the organics with a small content of BaCO₃ remaining. Cexs at 900 °C is formed through a single phase (La_{0.3}Ba_{0.7}Zr_{0.4}Co_{0.6}O_{3-δ}) at 715 °C in N₂. Cdir is formed at 1000 °C by calcination of the precursor. Green symbols represent composite by exsolution (Cexs) and orange symbols the direct composite (Cdir).

S2) after cooling the transient phase to room temperature as has also been reported for barium containing perovskites as BSFC²⁷.

The analysis of the diffractograms and the cell parameters obtained by Rietveld refinement of HTXRD data versus temperature are presented in Figure 5. During the formation of Cexs (green) an expansion of the SP cell parameter occurs prior to the exsolution. The BaZrO₃ (BZ)-based phase shows increasing cell parameter while for the La_{0.5}Ba_{0.5}CoO_{3-δ} (LB)-based phase a continuous decrease in the cell parameter is observed. The intermediate transient phase observed prior to the Cdir formation shows decreasing cell parameter to a minimum at ~700 °C increasing again until decomposition at ~800 °C. The transient phase decomposes into a composite where the cell parameters of both the LB- and BZ-based phases increase with increasing temperature. The cell parameters for each phase of both composites become equal at 1000 °C. Scanning electron micrographs of SP, Cexs and Cdir obtained from STEM are presented in Figure 6. SP consists of several μm large agglomerates while both Cexs and Cdir have agglomerate sizes in the range of 100-250 nm. Larger agglomerates are visible in the Cdir compared to the Cexs. The surface area of the Cexs and Cdir materials are 7.4 m²/g and 4.7 m²/g, respectively. Estimated average particle size from surface area assuming spherical and non-porous particles was 130 nm for Cexs and 204 nm for Cdir.

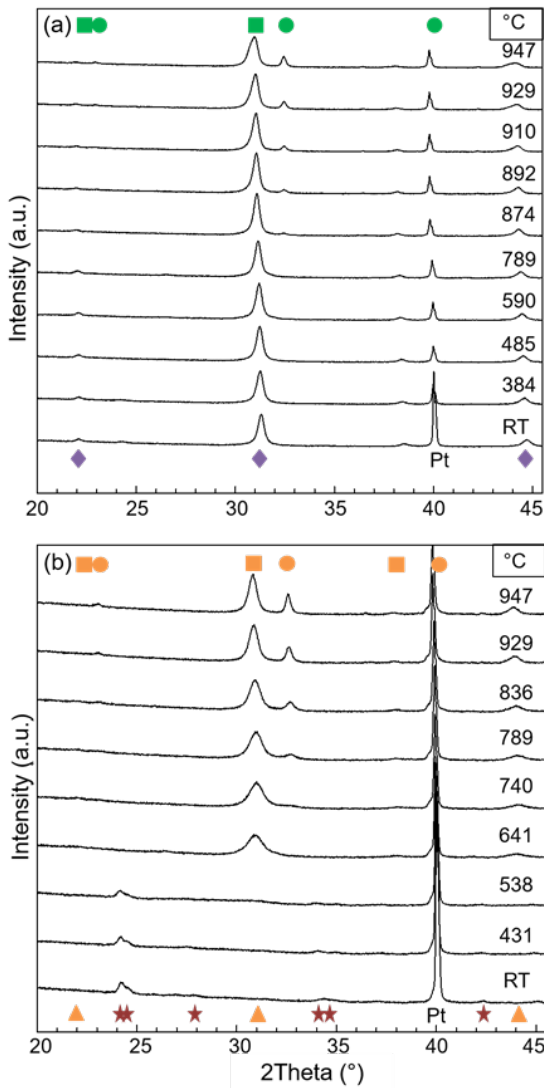


Figure 4. *In situ* HTXRD of (a) single phase ($\text{La}_{0.3}\text{Ba}_{0.7}\text{Zr}_{0.4}\text{Co}_{0.6}\text{O}_{3.8}$) and (b) precursor with BaCO_3 , during heating in synthetic air. A composite consisting of $\text{La}_{0.5}\text{Ba}_{0.5}\text{CoO}_{3.5}$ -based and a BaZrO_3 -based phase is formed in both experiments. A transient phase forms from 600 to 800 °C when heating the precursor phase. Green symbols represent composite by exsolution (Cexs) and orange symbols the direct composite (Cdir).

TEM micrographs in Figure 7 demonstrate that the 100-250 nm agglomerates observed in SEM contain smaller grains. The deconvolution of the agglomerates was done by high resolution image analysis (Figure S1). The Cexs agglomerates consist of a BZ-based grain matrix with embedded smaller LB-based grains with high degree of contiguity between the two phases and very low contiguity between the LB-based grains. An illustration of the grains (line-marked as guides for the eye) of both phases determined from high resolution images of different Cexs agglomerates is included in Figure 7 (a). The BZ-based phase consists of larger grains than the LB-phase with the average grain size of 45 nm compared to 20 nm for the LB-phase. The Cdir agglomerates consist of a mixture of BZ-based phase with an average grain size of 62 nm and LB-based phase with an average grain size of 48 nm with a high degree of contiguity between each phase. Histograms of the grain size distributions of Cexs and Cdir composites are shown in Figure 7 (b) and (d).

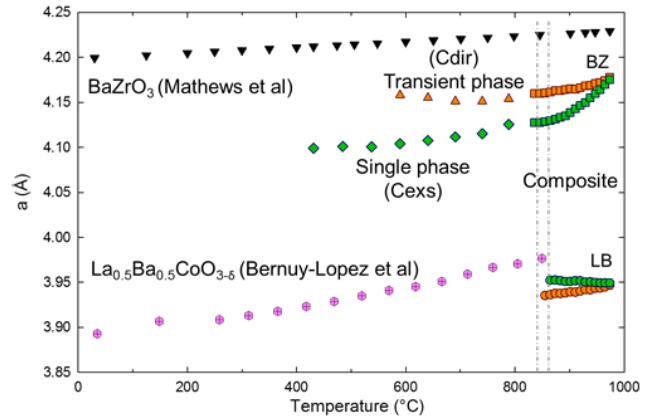


Figure 5. Cell parameters of single phase and composite by exsolution and transient phase and direct composite revealed from high temperature X-ray diffraction. Barium zirconate and lanthanum barium cobaltite cell parameters from the literature are included.

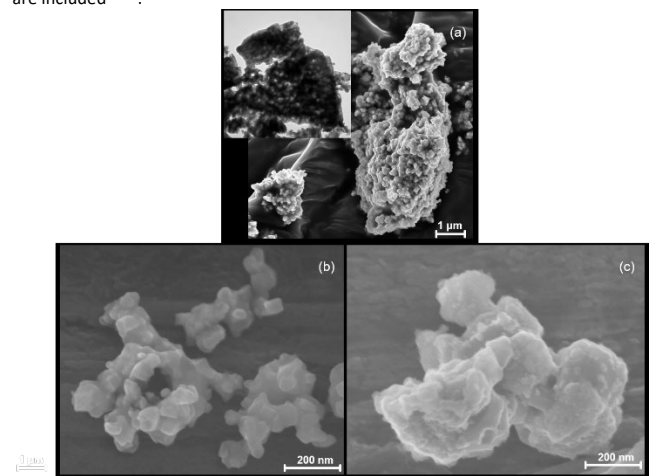


Figure 6. STEM images of (a) single phase reduced at 715 °C in N_2 and subsequently heat treated in ambient air at 900 °C (b) into the composite by exsolution and (c) direct composite heat treated at 1000 °C in ambient air. The insert in (a) shows a TEM image of single phase.

The grain size from HRTEM, particle size estimated from the surface area analysis, average agglomerate size by S(T)EM and crystallite size obtained by Rietveld analysis are compared in Table 1. Larger particle and crystallite sizes for the Cdir composite are observed by all methods. Similar agglomerate size obtained by S(T)EM and particle size from surface area demonstrates the low porosity of the agglomerates as confirmed by TEM.

EDS-TEM analysis of the Cexs and Cdir composites revealed the presence of Co in the BZ-phase. The Rietveld refinements of the

composite diffractograms at room temperature were conducted using $\text{La}_{1-x}\text{Ba}_x\text{CoO}_{3-\delta}$ and $\text{BaZr}_{1-y}\text{Co}_y\text{O}_{3-\delta}$ cubic is displayed in Figure 9 (conductivities are not corrected for the porosity) or in Figure S3 (conductivities corrected for the

Table 1. Comparison of particle and grain size with SD of composite by exsolution (Cexs) and direct composite (Cdir) composites measured by different techniques.

Composition	Particle or grain size (nm)			
	Cexs		Cdir	
	$\text{La}_{0.8}\text{Ba}_{0.2}\text{CoO}_{3-\delta}$	$\text{BaZr}_{0.6}\text{Co}_{0.4}\text{O}_{3-\delta}$	$\text{La}_{0.6}\text{Ba}_{0.4}\text{CoO}_{3-\delta}$	$\text{BaZr}_{0.8}\text{Co}_{0.2}\text{O}_{3-\delta}$
BET	130		200	
S(T)EM	100-150		150-250	
HRTEM	20±8	45±14	48±24	62±24
Rietveld analysis	42±23	55±22	78±28	91±33

perovskite structures and refining x and y variables, obtaining better fits than refining the nominal composition of the composites. Table 2 resumes the chemical composition of the Cexs and Cdir composites obtained by quantitative EDS-TEM analyses in combination with the XRD Rietveld refinements (Figure 8). The Cexs and Cdir composite compositions are 0.4 $\text{La}_{0.8}\text{Ba}_{0.2}\text{CoO}_{3-\delta}$ - 0.6 $\text{BaZr}_{0.6}\text{Co}_{0.4}\text{O}_{3-\delta}$ and 0.5 $\text{La}_{0.6}\text{Ba}_{0.4}\text{CoO}_{3-\delta}$ - 0.5 $\text{BaZr}_{0.8}\text{Co}_{0.2}\text{O}_{3-\delta}$, respectively. The thermal history of Cexs and Cdir is different and therefore gives final materials with different composition and microstructure. Both composites evolve from the same stoichiometry and will have the same average composition. The differences in phase composition in each composite is compensated by the molar ratio of the phases in the composite. The formation of a single phase under N_2 and further exsolution into the 2-phase composite (Cexs) evolves into a finer microstructure compared to Cdir. The exsolution process can be tailored to aim a target composition as shown in Fig. 5.

The DC-conductivity of 50 % dense Cexs and 70 % dense Cdir bars in dry O_2 , synthetic air and N_2 as a function of temperature

porosity with the Bruggeman model) The composite by exsolution shows a significantly lower conductivity compared to the composite formed by direct calcination. Cexs possesses a semiconducting behavior with increasing conductivity with increasing temperature independently on the atmosphere. The highest conductivity of 0.8 S/cm is observed at 800 °C in 1 atm O_2 . The conductivity decreases to 10^{-2} S/cm at room temperature at high $p\text{O}_2$ and 10^{-3} S/cm in N_2 . The conductivity of Cdir is higher than Cexs at all temperatures and $p\text{O}_2$, remaining 30 S/cm at room temperature and high $p\text{O}_2$. At low $p\text{O}_2$ the Cdir composite exhibits lower conductivity with a maximum of 22 S/cm at 200 °C and decreasing to 13 S/cm at room temperature.

The electrochemical performance of the composite cathodes in symmetric cells is shown in Nyquist plots for Cexs and Cdir in 3 % moist synthetic air at 400 and 600 °C in Figure 10. The diagrams were fitted with the equivalent circuit $\text{LRs}(\text{R}_1\text{Q}_1)(\text{R}_2\text{Q}_2)(\text{R}_3\text{Q}_3)$. The inductance of the device is represented by L and the ohmic resistance of the bulk electrolyte by R_s . R_i and Q_i are the polarization resistances and the constant phase elements of each process, respectively. The different processes were attributed to the electrolyte or electrode using the pseudo capacitances (C) ²⁸; R_1 corresponding to the grain boundary of the electrolyte $\text{C} \sim 10^{-9}$ F/cm², R_2 and R_3 to the electrode with $\text{C} \sim 10^{-5}$ F/cm² and $\text{C} \sim 10^{-2}$ F/cm². Figure 11 shows the ASR obtained from the EIS data for Cexs and Cdir in dry and moist conditions. Cexs has a better performance in wet conditions, with lower ASR at all temperatures compared to Cdir. The ASR is taken as the sum of R_2 and R_3 , the resistances assigned to the electrode. The ASR values are 1.54 and 1.76 $\Omega \cdot \text{cm}^2$ for Cexs and Cdir at 600 °C and 3 % H_2O , respectively. The ASR values from 400 to 600 °C in 3 % moist synthetic air for both cathode compositions is summarized in Table 3.

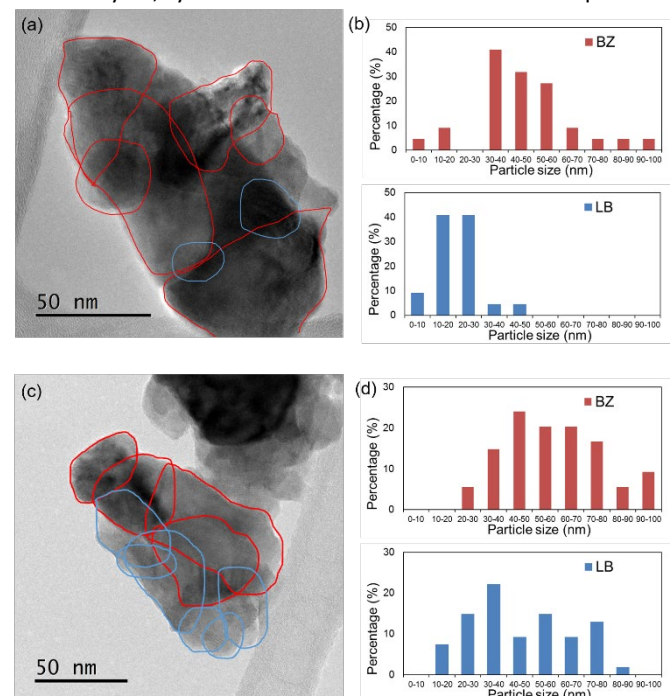


Figure 7. TEM micrographs of the composite by exsolution (a) and the direct composite (c). Agglomerates of BZ-based phase and LB-based phase are shown. The approximate circumference of the grains of BZ- (red) and LB-based phase (blue) are marked as guide for the eye. The grain size distribution is represented in (b) and (d) for each composite.

Discussion

Synthesis method

The synthesis was optimized by a systematic study of the complexing agent/cation ratio, complexing agent/oxidant ratio,

Table 2. Chemical analysis of composite by exsolution (Cexs) and direct composite (Cdir) measured by TEM-EDS. Nominal composition $\text{La}_{0.5}\text{Ba}_{0.5}\text{CoO}_{3-\delta}$ - BaZrO_3 is included in the table. The standard deviation is given based on several point analyses.

Phase	La	Ba	Zr	Co	O
$\text{La}_{0.5}\text{Ba}_{0.5}\text{CoO}_{3-\delta}$	0.5	0.5	--	1	3-6
BaZrO_3	--	1	1	--	3
LB-Cexs	0.95 ± 0.2	0.18 ± 0.05	--	1.08 ± 0.18	2.55 ± 0.4
BZ-Cexs	--	1.01 ± 0.05	0.66 ± 0.17	0.42 ± 0.09	2.9 ± 0.3
LB-Cdir	0.72 ± 0.08	0.43 ± 0.17	--	1.01 ± 0.10	2.8 ± 0.3
BZ-Cdir	--	0.95 ± 0.21	0.72 ± 0.21	0.22 ± 0.04	3.1 ± 0.3

pH of the solution and thermal treatment in order to obtain a fine solid state precursor. The complexing agent/cation ratio was critical with respect to obtain a stable sol prior to gelation. Cations were complexed with EDTA and CA in an optimized cation:EDTA:CA ratio of 1:1.5:3 to retain the cations complexed during evaporation of the solvent and gelation. A lower complexing agent content resulted in precipitation of barium and zirconyl ions as they have a very low solubility in water as well as a careful control and adjustment of the pH prevented the precipitation of these species before gelation^{29, 30}. Ba was complexed with EDTA, dissolved in NH_4OH at pH 10.5 for the deprotonation of the carboxylic acid groups, to avoid precipitation of barium upon evaporation of water.

The addition of the zirconyl solution with pH=1 was a critical step as it destabilized the solution. A precipitation occurred around the drop of the zirconyl solution but it instantaneously dissolved in the solution. The reversibility of the precipitation depended on the rate of the addition of the zirconyl solution. A rate higher than 1.5 mL/min made the precipitation irreversible. The optimized complexing agent:oxidant ratio of 2:1 promoted gelation and suppressed combustion at lower temperatures. Lower complexing agent:oxidant ratio derived in a combustion by smoldering of the gel³¹ forming pure barium zirconate at the early stage of the synthesis. The xerogel was formed by partial decomposition of the gel at 200 °C. The 85 wt.% loss observed due to evaporation of absorbed water and decomposition of the nitrates and organic gel network is in good agreement with the composition of the xerogel (Figure 2). The thermal treatment of the precursor material was adjusted taking into account the decomposition temperature of the nitrates and the complexing agents. The single phase was obtained at $715 \text{ °C} \pm 10 \text{ °C}$. Secondary phases were observed by XRD outside this temperature range. The exsolution into the Cexs composite was initiated at about 900 °C with the possibility to tailor the chemical composition depending on the applied thermal treatment. Cdir was prepared in one step at 1000 °C.

In situ exsolution of the single phase material

The formation of the Cexs composite from the precursor goes through the SP, which was stabilized in inert atmosphere. The SP was prepared at 715 °C in N_2 forming a cubic perovskite structure where La and Ba are accommodated at the A-site and

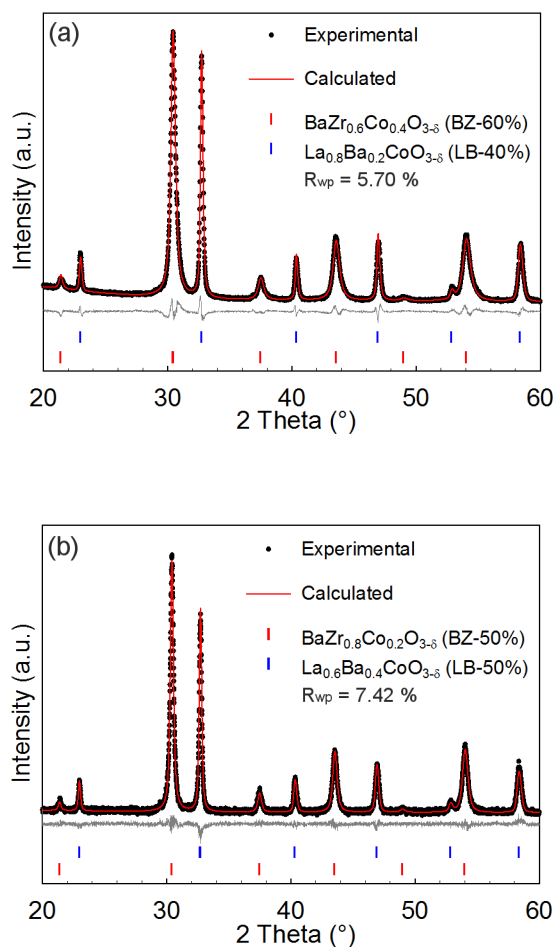


Figure 8. Rietveld refinement of the XRD data for composite by exsolution (a) and direct composite (b) using cubic Pm-3m space groups.

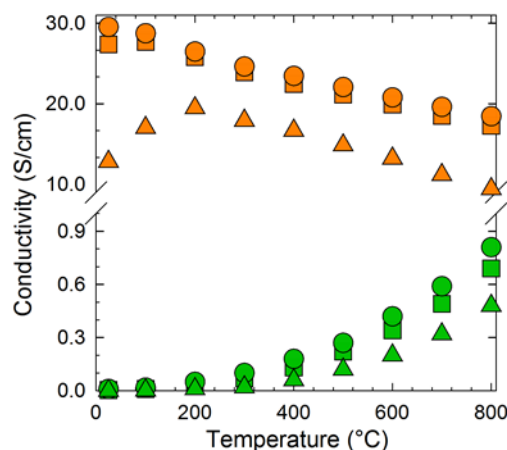


Figure 9. DC-conductivity of 50% dense composite by exsolution and 70% dense direct composite in dry and pure O_2 (circles), dry synthetic air (rectangles) and dry pure N_2 (triangles). Green symbols represent composite by exsolution (Cexs) and orange symbols the direct composite (Cdir).

Zr and Co at the B-site in the perovskite lattice. Cobalt is

Table 3. Cathode area specific resistance ($\Omega \cdot \text{cm}^2$) of the composite by exsolution and direct composite at various temperatures and $p_{\text{H}_2\text{O}} = 0.03 \text{ atm}$.

	ASR ($\Omega \cdot \text{cm}^2$)				
	400 °C	450 °C	500 °C	550 °C	600 °C
Cexs	18.11	7.63	4.52	2.74	1.54
Cdir	37.28	13.51	6.83	3.21	1.76

expected to be in the divalent state Co^{2+} at $p_{\text{O}_2} = 3.5 \cdot 10^{-4} \text{ atm}$ ³². The ionic radii of Co^{2+} (0.745 Å) is similar to Zr (0.72 Å)³³, which also explain why Co and Zr are disordered at the B-site. The SP is stable at room temperature when cooled in N_2 . The exposure of the SP phase to high p_{O_2} induces the oxidation of the cobalt to a mixture of $\text{Co}^{3+}/\text{Co}^{4+}$. This change in oxidation state induces the destabilization of the SP due to the mismatch in the ionic radii at the B-site, (Co^{3+} : 0.61 Å and Co^{4+} : 0.53 Å)³³. The decomposition of SP can be described by the hypothetical reaction, assuming that Co is not introduced into the BZ phase: $\text{La}_{0.3} \text{Ba}_{0.7} \text{Zr}_{0.4} \text{Co}_{0.6} \text{O}_{2.75-\delta} + \text{O}_2 \rightarrow 0.6 \text{La}_{0.5} \text{Ba}_{0.5} \text{CoO}_{3-\delta} + 0.4 \text{BaZrO}_3$.

However, the comparison of the cell parameters (Figure 6) with pure BaZrO_3 reveals that the BZ phase contains significant amount of Co on B site or La on A site³⁴. EDS analysis also confirmed the presence of Co in the BZ-phase which is in good agreement with HTXRD data where the reduction of the cell parameter is due to the smaller ionic radii of the Co^{3+} (0.61 Å) and Co^{4+} (0.53 Å) compared to zirconium (0.72 Å).

Hence, the exsolution of SP gives a composite consisting of $\text{La}_{1-x} \text{Ba}_x \text{CoO}_{3-\delta}$ and $\text{BaZr}_{1-y} \text{Co}_y \text{O}_{3-\delta}$ with the possibility to tailor the stoichiometry of the composite controlling the thermal history and to extend the method to more complex systems as it was shown in our recent work²¹. The initial SP transformed gradually into the BZ phase remaining rich in barium and zirconium and hosting about 40 at% cobalt at the B-site at 900 °C. An almost constant cell parameter was observed during the exsolution of the LB-based phase of the Cexs composite up to 900 °C. This indicates that the nucleation of the LB-phase occurred by diffusion of La, Ba and Co out of the SP phase with a constant rate during exsolution while the small lattice parameter differences are attributed to the Ba content. The

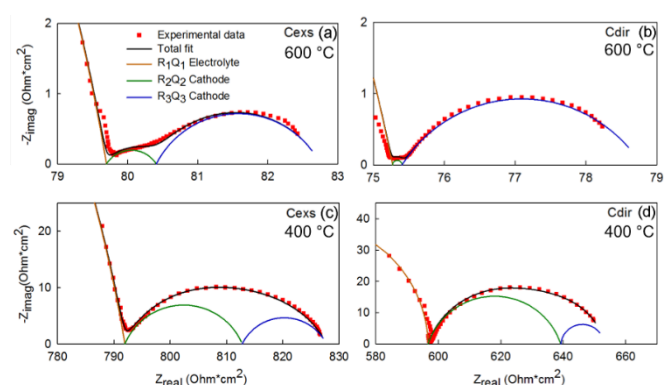


Figure 10. Nyquist plots of symmetrical cells with spray coated composite by exsolution (a, c) and direct composite (b and d) cathodes in synthetic air with $p_{\text{H}_2\text{O}} = 0.03 \text{ atm}$ at 600 (a, b) and 400 °C (c, d). The dotted line corresponds to the experimental data and the solid lines to the fits. The equivalent circuit used for fitting is $\text{LRs}(\text{R}_1\text{Q}_1)(\text{R}_2\text{Q}_2)(\text{R}_3\text{Q}_3)$.

change of the composition of the phases imposes a change in the composite phase ratio. The exsolved LB phase contains La with 20 at% of the A-site occupied by Ba and cobalt at the B-site at 900 °C. EDS analysis of Cexs prepared at 900 °C showed no La in the BZ-phase and no Zr in the LB-phase. Further heat treatment above 900 °C promoted Co and Ba diffusion from BZ-phase to LB-phase occupying La with 40 at% of the A-sites by Ba at 1000 °C.

Rietveld refinements of Cexs confirmed that the BZ-based phase has the cubic $Pm-3m$ structure (Figure 8). The LB phase with barium content below 35 at% on A-site has been attributed to the $R-3c$ rhombohedral crystal structure³⁵⁻³⁷. No additional reflections nor splitting of the peaks related to the rhombohedral structure could be observed in this work. Good fits were obtained for both $Pm-3m$ ($R_{\text{wp}} = 5.70 \%$) and $R-3c$ ($R_{\text{wp}} = 6.02 \%$) space groups. No clear conclusion about the crystal structure of $\text{La}_{0.8} \text{Ba}_{0.2} \text{CoO}_{3-\delta}$ can be made without further experiments but the nanostructure of the material could explain the cubic structure of the Cexs LB-phase.

Composite by direct calcination

A transient phase was formed during the preparation of the Cdir material. An oxygen driven phase separation of the transient phase derived into the composite formation at 1000 °C. This different formation mechanism of the composite is confirmed by Rietveld refinements of HTXRD in Figure 5 where, unlike Cexs, LB-phase shows an increase of the cell parameter. A composite with two phases, LB- and BZ- based phases, was only obtained at 1000 °C, 100 °C higher than Cexs. Lower heat treatment temperatures resulted in secondary phases upon cooling to room temperature with the formation of BaCO_3 or hexagonal BaCoO_x polymorphs. The formation temperature at 1000 °C induced a change in the proportion and composition of the two phases leading to a $0.5 \text{La}_{0.6} \text{Ba}_{0.4} \text{CoO}_{3-\delta} - 0.5 \text{BaZr}_{0.8} \text{Co}_{0.2} \text{O}_{3-\delta}$ composite. The Cdir route enables the preparation of the composite in one calcination step but it is not possible to tailor the composition nor the composite ratio in the same manner as the Cexs without the appearance of secondary phases. BZ and LB-phases were successfully refined with $Pm-3m$ cubic structure (Figure 8 (b)). LB-phase with Ba content of 40 at% on the A-site is reported to be pseudocubic $Pm-3m$ or $R-3c$ depending on the size of the crystals^{10, 38}.

Microstructure

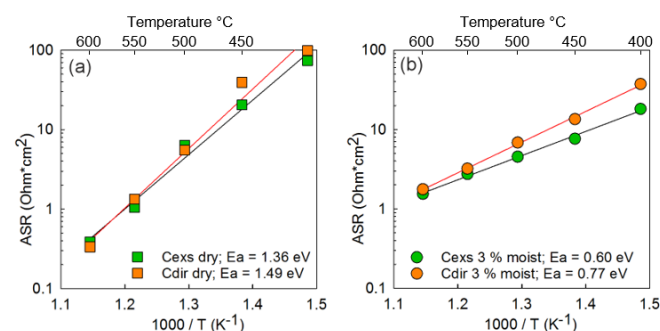


Figure 11. Total area specific resistance (ASR) corresponding to the composite by exsolution and direct composite cathodes in symmetric cell configuration in (a) dry and (b) 3 % moist synthetic air in an Arrhenius diagram as a function of temperature.

Large single grains of about 200 nm were observed in SP by TEM (in-set in Figure 6(a)). Cexs on the other hand consisted of smaller grains compared to SP, which implies a breakdown of the single phase in smaller grains. This may be the reason for single and isolated LB-phase grains to be trapped inside the BZ-matrix as the LB-phase exsolves at the interfaces. A large difference in contiguity is observed for the two composites. The microstructure of Cdir, with more equal grain size and with a high degree of contiguity for the two phases might be explained by the oxygen driven formation of this composite. The difference in the final microstructure of the two composites corroborates the different formation mechanism of the composites.

Electrochemical properties

The total electrical conductivity presented in Figure 9 shows significantly higher values for the Cdir composite compared to the Cexs. The minimum electronic conductivity required for a cathode in PCFC is 1 S/cm for a dense cathode^{3,39}. Applying the Bruggeman model⁴⁰, Cexs fulfills the PCFC cathode requirement with a conductivity of 1 S/cm at 500 °C (Figure S3). Undoped BaZrO₃ is reported to have a total electrical conductivity of 10⁻² Scm⁻¹ at 1000 °C⁴¹. This means that the major contribution to the electrical conductivity for the composites comes either from the LB-phase or the cobalt doping of the BZ-phase and it depends on the contiguity of the phases.

The electrical conductivity of Cdir corresponds to p-type semiconducting behavior reported in the literature^{32,45,46}. The decrease in conductivity below 200 °C is characteristic of a metal-insulator M-I transition, which occurs due to an ordering

composite is expected to be due to the continuous LB-phase with high degree of contiguity.

Cexs shows electronic conduction with semiconducting behavior as reported for La_{0.8}Ba_{0.2}CoO_{3-δ}⁴⁹. The lower conductivity of Cexs compared to Cdir can be explained by several factors. The lower electronic conductivity of the Cexs composite can be explained by the presence of Co with mixed valence, transferring the Co-doped BZ an electronic conductor, and the low contiguity between the major electronic conducting LB-phase. Further, the chemical composition of the matrix, with a significant amount of Co in the BZ-phase becomes the phase charge carrier for the Cexs composite. The higher electrical conductivity of Cdir compared to Cexs can be explained due to the higher contiguity of the LB-phase, the main charge carrier. This difference in phase contiguity derives from the composite preparation method, giving different microstructures and therefore, significative difference in electrical conductivity.

Both composites show similar activation energies and ASR in symmetrical cells under dry conditions which is in good agreement with studies on the La_{1-x}Ba_xCoO_{3-δ} family of materials where a very good performance was observed for intermediate temperature SOFC^{10,12,50}. At the same time, the B-site of the BZ-phase is substituted by Co in both composites, which is potentially active as proton conductor⁵¹. The ASR of both composites increased as the temperature decreased. Above 550 °C, the ASR of both electrodes in dry conditions was significantly lower than in moist conditions. Unlike the dry conditions, the ASR of the two cathodes decreased below 500 °C in 3 % moist synthetic air. Better performance was found for Cexs with an E_a as low as 0.60 eV in moist conditions compared

Table 4. Comparison of the cathode area specific resistance from the literature in 3 % moist synthetic air⁽¹⁾, oxygen⁽²⁾ or hydrogen⁽³⁾ at 600 °C in symmetric cell configuration.

Cathode material	Electrolyte	Cathode deposition method	ASR (Ω · cm ²)	Activation energy (eV)	Ref.
La _{0.8} Ba _{0.2} CoO _{3-δ} BaZr _{0.6} Co _{0.4} O _{3-δ} (40:60 by weight)	BaZr _{0.9} Y _{0.1} O _{3-δ}	Spray coating	1.54 ⁽¹⁾	0.60	This work
La _{0.6} Ba _{0.4} CoO _{3-δ} BaZr _{0.8} Co _{0.2} O _{3-δ} (50:50 by weight)	BaZr _{0.9} Y _{0.1} O _{3-δ}	Spray coating	1.76 ⁽¹⁾	0.77	This work
La _{0.6} Ba _{0.4} (CoFeMn)O _{3-δ} BaZr _{0.6} (CoFeMn) _{0.4} O _{3-δ} (43:57 by weight)	BaZr _{0.9} Y _{0.1} O _{3-δ}	Screen printing	0.44 ⁽¹⁾	1.1	21
Ba _{0.5} Sr _{0.5} Co _{0.8} Fe _{0.2} O _{3-δ} -BaCe _{0.9} Y _{0.1} O _{3-δ} (70:30 by weight)	BaCe _{0.9} Y _{0.1} O _{3-δ}	Painting of slurry	0.53 ⁽²⁾	-	42
BaCo _{0.4} Fe _{0.4} Zr _{0.1} Y _{0.1} O _{3-δ}	BaCe _{0.7} Zr _{0.1} Y _{0.1} Yb _{0.1} O _{3-δ} /1%wt.NiO	Screen printing	~0.4 ⁽²⁾	~ 0.74	3
BaZr _{0.1} Ce _{0.7} Y _{0.1} Yb _{0.1} O _{3-δ} -60Nd _{1.95} NiO _{4+δ}	BaCe _{0.7} Zr _{0.1} Y _{0.1} Yb _{0.1} O _{3-δ}	Screen printing	7.16 ⁽¹⁾	0.66	4
La ₂ NiO _{4+δ} -LaNi _{0.6} Fe _{0.4} O _{3-δ}	BaZr _{0.1} Ce _{0.7} Y _{0.2} O _{3-δ}	Painting of slurry	~ 10.8 ⁽³⁾	1.23	43
BaGd _{0.8} La _{0.2} Co ₂ O _{6-δ}	BaZr _{0.7} Ce _{0.2} Y _{0.1} O _{3-δ}	Drop casting + screen printing	0.2 ⁽²⁾	~ 0.78	44
LaCoO ₃	BaZr _{0.7} Ce _{0.2} Y _{0.1} O _{3-δ}	Infiltration into porous backbone	0.14 ⁽¹⁾	-	15
La _{0.58} Sr _{0.4} Co _{0.2} Fe _{0.8} O _{3-δ}	BaZr _{0.7} Ce _{0.2} Y _{0.1} O _{3-δ}	Infiltration into porous backbone	0.98 ⁽¹⁾	-	9
La _{0.58} Sr _{0.4} Co _{0.2} Fe _{0.8} O _{3-δ}	BaZr _{0.7} Ce _{0.2} Y _{0.1} O _{3-δ}	Spray pyrolysis	0.89 ⁽¹⁾	-	9
La _{0.6} Sr _{0.4} Co _{0.2} Fe _{0.8} O _{3-δ} /BaCe _{0.9} Yb _{0.1} O _{3-δ} composite (1:1 by weight)	BaCe _{0.8} Y _{0.2} O _{3-δ}	Painting of slurry	~ 1.1 ⁽¹⁾	-	18

of the low spin Co^{III} ($t_{2g}^5 e_g^0$) and intermediate spin Co^{III} ($t_{2g}^5 e_g^1$) ions⁴⁷. The Cdir material shows p-type conductor behavior from 200 to 800 °C⁴⁸. The good electrical conductivity of this

to Cdir (E_a = 0.77 eV).

In the impedance spectra (Figure 10), two main processes can be assigned to the cathode; the charge transfer and oxygen dissociation/adsorption. It is widely reported in the cathode

literature that the middle range frequency process related to the charge transfer and the low frequency process to the oxygen dissociation/adsorption^{52, 53}. The ASR is dominated by the low frequency process at 600 °C and by the middle frequency process at 400 °C. The utilization of composite cathodes usually decreases the polarization resistance compared to the single phase. The ASR of the composite cathodes in this work is compared to the state of the art cathodes in Table 4. The polarization resistances obtained for Cexs in this study are very promising, achieving among the lowest activation energy reported in the literature. In addition, further optimization is in progress. As most of the composite cathodes reported consist of a larger weight percent of the cathode material, the change of the composite ratio is very promising for obtaining high-performance cathodes for PCFCs.

Conclusions

Composite cathodes Cexs and Cdir based on $\text{La}_{0.5}\text{Ba}_{0.5}\text{CoO}_{3-\delta}$ - BaZrO_3 (LB-BZ) nominal composition were successfully synthesized by exsolution of a $\text{La}_{0.3}\text{Ba}_{0.7}\text{Zr}_{0.4}\text{Co}_{0.6}\text{O}_{3-\delta}$ single phase or direct calcination of the precursor made by a modified Pechini sol-gel synthesis. The new exsolution approach enables to tailor the chemical composition of the cathode composite by the thermal treatment. The composite composition differences between exsolution and direct calcination were analyzed and carefully discussed. The single phase exsolved to 0.4 $\text{La}_{0.8}\text{Ba}_{0.2}\text{CoO}_{3-\delta}$ - 0.6 $\text{BaZr}_{0.6}\text{Co}_{0.4}\text{O}_{3-\delta}$ Cexs composite while a direct calcination of the precursor evolved to 0.5 $\text{La}_{0.6}\text{Ba}_{0.4}\text{CoO}_{3-\delta}$ - 0.5 $\text{BaZr}_{0.8}\text{Co}_{0.2}\text{O}_{3-\delta}$, composite. The change in composite molar ratio, the chemical composition and thermal history derived in a different microstructure for the two composites. Cexs consisted of a BZ matrix and exsolved LB-phase with finer grain size while Cdir consisted of larger grains with higher contiguity between the two phases. Both composites fulfill the 1 S/cm electrical conduction requirement for PCFC cathode application, hence, the higher electrical conductivity of the Cdir composite was attributed to the different nanostructure of the composites and the higher degree of contiguity of the LB-phase. Electrochemical characterization of symmetrical cells with Cexs cathodes showed very promising results with an ASR as low as 18 Ω cm² at 400 °C and 1.54 Ω cm² at 600 °C with $E_a = 0.60$ eV. The present results show the potential of the synthesis by exsolution and further optimization of the microstructure and deposition method is expected to further increase the cathode performance.

Acknowledgments

Financial support from The Research Council of Norway under the program NANO2021 to the project (number 228355) "Functional oxides for clean energy technologies: fuel cells, gas separation membranes and electrolyzers" (FOX CET) conducted by SINTEF Materials and Chemistry, University of Oslo and The Norwegian University of Science and Technology (NTNU) in Trondheim, is gratefully acknowledged. The TEM work was carried out on the NORTEM JEOL JEM-2100F, TEM Gemini Centre, NTNU, Norway.

Conflicts of interest

The authors declare no conflict of interest.

Author Contributions

All authors conceived and designed the experiments; analyzed the data and revised the paper. L.R-M. performed the experiments and wrote the original draft of the paper.

References

1. J. W. Fergus, *J Power Sources*, 2006, **162**, 30-40.
2. K. D. Kreuer, *Annu Rev Mater Res*, 2003, **33**, 333-359.
3. C. C. Duan, J. H. Tong, M. Shang, S. Nikodemski, M. Sanders, S. Ricote, A. Almansoori and R. O'Hayre, *Science*, 2015, **349**, 1321-1326.
4. C. Y. Yang, X. X. Zhang, H. L. Zhao, Y. N. Shen, Z. H. Du and C. J. Zhang, *Int J Hydrogen Energy*, 2015, **40**, 2800-2807.
5. M. Ni, M. K. H. Leung and D. Y. C. Leung, *Fuel Cells*, 2007, **7**, 269-278.
6. J. Suntivich, H. A. Gasteiger, N. Yabuuchi, H. Nakanishi, J. B. Goodenough and Y. Shao-Horn, *Nat Chem*, 2011, **3**, 546-550.
7. Z. P. Shao and S. M. Haile, *Nature*, 2004, **431**, 170-173.
8. J. Dailly, S. Fourcade, A. Largeteau, F. Mauvy, J. C. Grenier and M. Marrony, *Electrochim Acta*, 2010, **55**, 5847-5853.
9. S. Ricote, N. Bonanos, P. M. Rorvik and C. Haavik, *J Power Sources*, 2012, **209**, 172-179.
10. C. Setevich, L. Moggi, A. Caneiro and F. Prado, *J Electrochem Soc*, 2012, **159**, B73-B80.
11. H. Zhao, Q. Li and L. P. Sun, *Sci China Chem*, 2011, **54**, 898-910.
12. C. Bernuy-Lopez, L. Rioja-Monllor, T. Nakamura, S. Ricote, R. O'Hayre, K. Ameszawa, M.-A. Einarsrud and T. Grande, *Materials*, 2018, **11**, 196.
13. J. H. Kim and A. Manthiram, *J Electrochem Soc*, 2008, **155**, B385-B390.
14. R. Zohourian, R. Merkle, G. Raimondi and J. Maier, 2018, **28**, 1801241.
15. S. Ricote, N. Bonanos, F. Lenrick and R. Wallenberg, *J Power Sources*, 2012, **218**, 313-319.
16. C. Duan, D. Hook, Y. Chen, J. Tong and R. O'Hayre, *Energy Environ Sci*, 2017, **10**, 176-182.
17. S. P. Jiang, *Int J Hydrogen Energy*, 2012, **37**, 449-470.
18. E. Fabbri, S. Licocchia, E. Traversa and E. D. Wachsman, *Fuel Cells*, 2009, **9**, 128-138.
19. G. Taillades, P. Pers, V. Mao and M. Taillades, *Int J Hydrogen Energy*, 2016, **41**, 12330-12336.
20. G. E. Syvertsen, 2012:165, Norwegian University of Science and Technology, Faculty of Natural Sciences and Technology, Department of Materials Science and Engineering, 2012.
21. L. Rioja-Monllor, S. Ricote, C. Bernuy-Lopez, T. Grande, R. O'Hayre and M.-A. Einarsrud, *Inorganics*, 2018, **6**, 83.
22. D. Papargyriou and J. T. S. Irvine, *Solid State Ionics*, 2016, **288**, 120-123.
23. L. Thommy, O. Joubert, J. Hamon and M. T. Caldes, *Int J Hydrogen Energy*, 2016, **41**, 14207-14216.
24. G. Tsekouras, D. Neagu and J. T. S. Irvine, *Energy Environ Sci*, 2013, **6**, 256-266.
25. J. Zhou, T. H. Shin, C. S. Ni, G. Chen, K. Wu, Y. H. Cheng and J. T. S. Irvine, *Chem Mater*, 2016, **28**, 2981-2993.
26. R. Sažinas, C. Bernuy-López, M.-A. Einarsrud and T. Grande, *J Am Ceram Soc*, 2016, DOI: 10.1111/jace.14395, n/a-n/a.

27. M. G. Sahini, J. R. Tolchard, K. Wiik and T. Grande, *Dalton T*, 2015, **44**, 10875-10881.
28. J. R. Macdonald, *Solid State Ionics*, 1984, **13**, 147-149.
29. J. Kragten, *Berichte der Bunsengesellschaft für physikalische Chemie*, 1978, **82**, 1117-1118.
30. M. Sletnes, S. L. Skjærvø, M. Lindgren, T. Grande and M.-A. Einarsrud, *J Sol-Gel Sci Techn*, 2016, **77**, 136-144.
31. I. Kaus, P. I. Dahl, J. Mastin, T. Grande and M. A. Einarsrud, *J Nanomater*, 2006, DOI: Artn 49283 10.1155/Jnm/2006/49283.
32. C. Bernuy-Lopez, K. Høydalsvik, M. A. Einarsrud and T. Grande, *Materials*, 2016, **9**.
33. R. D. Shannon, *Acta Crystallogr A*, 1976, **32**, 751-767.
34. M. D. Mathews, E. B. Mirza and A. C. Momin, *J Mater Sci Lett*, 1991, **10**, 305-306.
35. W. J. Luo and F. W. Wang, *Powder Diffr*, 2006, **21**, 304-306.
36. A. P. Sazonov, I. O. Troyanchuk, H. Gamari-Seale, V. V. Sikolenko, K. L. Stefanopoulos, G. K. Nicolaides and Y. K. Atanassova, *Journal of Physics: Condensed Matter*, 2009, **21**, 156004.
37. C. Setevich, L. Mogni, A. Caneiro and F. Prado, *J Electrochem Soc*, 2011, **159**, B72-B79.
38. P. Mandal, P. Choudhury, S. K. Biswas and B. Ghosh, *Phys Rev B*, 2004, **70**, 104407.
39. Z. Wang, W. Yang, S. P. Shafi, L. Bi, Z. Wang, R. Peng, C. Xia, W. Liu and Y. Lu, *J Mater Chem A*, 2015, **3**, 8405-8412.
40. D. A. G. Bruggeman, *Annalen der Physik*, 1935, **416**, 636-664.
41. H. Iwahara, T. Yajima, T. Hibino, K. Ozaki and H. Suzuki, *Solid State Ionics*, 1993, **61**, 65-69.
42. G. Taillades, P. Pers, P. Batocchi and M. Taillades, *Ecs Transactions*, 2013, **57**, 1289-1296.
43. J. Hou, J. Qian, L. Bi, Z. Gong, R. Peng and W. Liu, *J Mater Chem A*, 2015, **3**, 2207-2215.
44. R. Strandbakke, V. A. Cherepanov, A. Y. Zuev, D. S. Tsvetkov, C. Argiris, G. Sourkouni, S. Prunte and T. Norby, *Solid State Ionics*, 2015, **278**, 120-132.
45. D. Garces, C. F. Setevich, A. Caneiro, G. J. Cuello and L. Mogni, *J Appl Crystallogr*, 2014, **47**, 325-334.
46. J. H. Kim, L. Mogni, F. Prado, A. Caneiro, J. A. Alonso and A. Manthiram, *J Electrochem Soc*, 2009, **156**, B1376-B1382.
47. Y. Moritomo, M. Takeo, X. J. Liu, T. Akimoto and A. Nakamura, *Phys Rev B*, 1998, **58**, 13334-13337.
48. R. Amin and K. Karan, *J Electrochem Soc*, 2010, **157**, B285-B291.
49. M. S. Khalil, *Materials Science and Engineering: A*, 2003, **352**, 64-70.
50. C. Setevich, F. Prado and D. Z. de Florio, *Int J Hydrogen Energ*, 2014, **39**, 8738-8743.
51. M. A. Azimova and S. McIntosh, *Solid State Ionics*, 2009, **180**, 160-167.
52. J. Dailly, F. Mauvy, M. Marrony, M. Pouchard and J.-C. Grenier, *J Solid State Electr*, 2011, **15**, 245-251.
53. A. Grimaud, F. Mauvy, J. M. Bassat, S. Fourcade, L. Rocheron, M. Marrony and J. C. Grenier, *J Electrochem Soc*, 2012, **159**, B683-B694.